

Cite this: *RSC Adv.*, 2019, 9, 4682

Effect of initial support particle size of MnO_x/TiO₂ catalysts in the selective catalytic reduction of NO with NH₃†

Yang Yang,^{ab} Zhun Hu,^{id}*^a Rongli Mi,^a Dan Li,^a Xiang Yong,^a Huie Yang^b and Kunfeng Liu^b

A series of manganese-based catalysts supported by 5–10 nm, 10–25 nm, 40 nm and 60 nm anatase TiO₂ particles was synthesized *via* an impregnation method to investigate the effect of the initial support particle size on the selective catalytic reduction (SCR) of NO with NH₃. All catalysts were characterized by transmission electron microscopy (TEM), N₂ physisorption/desorption, X-ray diffraction (XRD), temperature programmed techniques, X-ray photoelectron spectroscopy (XPS) and *in situ* diffuse reflectance infrared transform spectroscopy (DRIFTS). TEM results indicated that the particle sizes of the MnO_x/TiO₂ catalysts were similar after the calcination process, although the initial TiO₂ support particle sizes were different. However, the initial TiO₂ support particle sizes were found to have a significant influence on the SCR catalytic performance. XPS and NH₃-TPD results of the MnO_x/TiO₂ catalysts illustrated that the surface Mn⁴⁺/Mn molar ratio and acid amount could be influenced by the initial TiO₂ support particle sizes. The order of surface Mn⁴⁺/Mn molar ratio and acid amount over the MnO_x/TiO₂ catalysts was as follows: MnO_x/TiO₂(10–25) > MnO_x/TiO₂(40) > MnO_x/TiO₂(60) > MnO_x/TiO₂(5–10), which agreed well with the order of SCR performance. *In situ* DRIFTS results revealed that the NH₃-SCR reactions over MnO_x/TiO₂ at low temperature occurred *via* a Langmuir–Hinshelwood mechanism. More importantly, it was found that the bridge and bidentate nitrates were the main active substances for the low-temperature SCR reaction, and bridge nitrate adsorbed on Mn⁴⁺ showed superior SCR activity among all the adsorbed NO_x species. The variation of the initial TiO₂ support particle size over MnO_x/TiO₂ could change the surface Mn⁴⁺/Mn molar ratio, which could influence the adsorption of NO_x species, thus bringing about the diversity of the SCR catalytic performance.

Received 7th December 2018
Accepted 19th January 2019

DOI: 10.1039/c8ra10077b

rsc.li/rsc-advances

1 Introduction

Nitrogen oxides (NO_x), as a harmful exhaust emission, can induce various human health and environmental hazards, such as acid rain, photochemical smog, and ozone layer depletion.^{1,2} Increasing attention has been focused on NO_x abatement, including NO_x storage-reduction (NSR or LNT),^{3–5} NO_x decomposition, and Selective Catalytic Reduction (SCR).^{6–8} SCR technology has been regarded as the most promising way to remove NO_x, and has been commercially applied in diesel engines and power plants. However, due to increasingly strict emission legislation, it is crucial to develop

future catalysts for low-temperature NO_x abatement techniques, to meet future exhaust gas emission legislation.⁹

Because of their various valence states and low cost, transition metal oxides (MnO_x, FeO_x, CoO_x, CuO_x), are usually used as catalysts in SCR research.^{6–18} Owing to their inherent instability and poor anti-sintering ability, transition metal oxides are usually supported on an “inert” support to enhance their thermal stability and catalyst lifespan. Pena *et al.*¹⁹ investigated low-temperature SCR using VO_x, CrO_x, MnO_x, FeO_x, CoO_x, NiO_x and CuO_x catalysts supported on TiO₂. The SCR activity for the various transition metal oxides as active sites supported on TiO₂ decreased in the following order: MnO_x > CuO_x ≥ CrO_x ≥ CoO_x > FeO_x >> VO_x >>> NiO_x, indicating that MnO_x was the most promising catalyst for future practical applications. Among supported catalysts, the properties of the support and the interaction between MnO_x and the support are often considered to be the main parameters affecting the catalytic activity. Smirniotis *et al.*²⁰ synthesized a series of manganese oxides supported on TiO₂, Al₂O₃, and SiO₂ to investigate the influence of the support on SCR activity with a space velocity 8000 h^{−1}. They found that the SCR activity of the supported MnO_x

^aInstitute of Industrial Catalysis, School of Chemical Engineering and Technology, Xi'an Jiaotong University, Xi'an, Shaanxi 710049, China. E-mail: huzhun@mail.xjtu.edu.cn; Fax: +86-29-82663189; Tel: +86-29-82663189

^bSinochem Modern Environmental Protection Chemicals (Xi'an) Co. LTD., Xi'an, Shaanxi 710201, China

† Electronic supplementary information (ESI) available. See DOI: 10.1039/c8ra10077b



catalysts decreased in the following order: TiO_2 (anatase) > SiO_2 > TiO_2 (rutile) > TiO_2 (anatase, rutile) > $\gamma\text{-Al}_2\text{O}_3$. $\text{MnO}_x/\text{TiO}_2$ (anatase) showed excellent NO_x abatement activity, even at 120°C when it reached complete conversion. Therefore, $\text{MnO}_x/\text{TiO}_2$ catalysts have been investigated on the basis of the effects of the preparation method,²¹ manganese precursors²² and manganese loading²³ on SCR activity.^{19,24} However, the interaction between manganese oxides and TiO_2 has not been fully investigated, especially on the effect of the support size.

The interaction between the active component and the support is not only influenced by the support type, but also relies on the size of the support.^{25–30} Soykal *et al.*³⁰ studied the effect of support particle size in steam reforming of ethanol over $\text{CoO}_x/\text{CeO}_2$ catalysts with CeO_2 support particle sizes in the micro- and nano-range. $\text{CoO}_x/\text{CeO}_x$ with smaller CeO_2 particle sizes manifested superior catalytic performance and coking resistance ability. These results can be ascribed to a combination of factors, including reducibility, dispersion and redox sites on the catalyst surface. All of these properties could be affected by the particle size of the support, thus leading to different catalytic performances. Pakulska *et al.*²⁸ investigated the effect of support particle size over NiO/ZrO_2 and NiO/CeO_2 on the catalytic oxidation of methane. They found that zirconia particles size could change the number of catalytic sites *via* varying the pre-exponential factor and ceria size could change the reaction activation energy by varying oxygen transport to the active sites. Xu *et al.*^{25–27} studied a series of Ni/ZrO_2 catalysts with various ZrO_2 particle sizes to systematically investigate the effect of support particle size on the reforming of methane with CO_2 . Their proposed nanocomposite catalyst, which could be defined as a catalyst with comparable Ni metal and zirconia nanocrystals, showed superior catalytic activity and long-term stability. They attributed this excellent catalytic performance to the boundary or perimeter between Ni and ZrO_2 , which could easily be generated by similar-sized Ni and ZrO_2 particles. All of the above examples illustrate that the support size can significantly influence the catalytic performance and catalyst lifespan, by affecting the properties of active sites or the boundary between active sites and the support. However, up until now, corresponding research regarding the effect of support size on NO_x abatement has rarely been reported.

In this work, a series of $\text{MnO}_x/\text{TiO}_2$ catalysts was prepared *via* an impregnation method with a variation of TiO_2 support particle sizes to investigate the effect of the initial TiO_2 support size on the SCR performance. In addition, these catalysts were characterized by N_2 physisorption, TEM, XRD, H_2 -TPR, O_2 -TPD, XPS and DRIFTS, to understand the effects of the structure, redox properties and active site-support interaction on the SCR catalysis.

2 Experimental

2.1 Preparation of catalysts

Anatase TiO_2 particles of various sizes (Aladdin Reagent Co., Ltd.) were used as support materials without any purification. All of the catalysts were synthesized *via* a wet impregnation method. In a typical process, 2 g TiO_2 with various particle sizes

and 0.84 mL 50 wt% $\text{Mn}(\text{NO}_3)_2$ (Tianjin Fuchen chemical reagents company) were added into 20 mL deionized water, and the mixture was vigorously stirred for 24 h at room temperature. Then the solution was dried under vacuum at 60°C in a rotary evaporator. The obtained powder was dried at 110°C overnight, and then calcined at 550°C for 5 h with a heating rate of 1°C min^{-1} in a muffle furnace. The obtained materials were denoted as $\text{MnO}_x/\text{TiO}_2(n)$, where n represents the particle size of TiO_2 . The actual manganese loading of the catalysts was determined by X-ray fluorescence spectrometry (XRF).

2.2 Catalytic test

A catalytic performance test for the NH_3 -SCR reaction was implemented in a fixed-bed plug-flow stainless-steel tubular reactor ($L = 60$ cm, $\Phi_{\text{in}} = 7$ mm). The typical components of the simulated gas were as follows: 500 ppm NO , 500 ppm NH_3 , 5 vol% O_2 and balance Ar with a space velocity of $40\,000\text{ mL g}^{-1}\text{ h}^{-1}$. The reaction temperature was recorded by a K-type thermocouple located inside the tube near the catalyst bed. Prior to the SCR catalytic measurements, the catalyst was pretreated in 20 vol% O_2/Ar at 400°C for 1 h. The reaction was carried out from 50°C to 350°C with an increment of 25°C and each temperature was held for 1 h to obtain a stable reaction conversion. The concentration of NO_x was detected by a fuel analyzer (AFRISO, M 60). NO_x conversion was calculated using the following equation:

$$\text{NO}_x \text{ conversion (\%)} = \frac{[\text{NO}_x]_{\text{in}} - [\text{NO}_x]_{\text{out}}}{[\text{NO}_x]_{\text{in}}} \times 100$$

2.3 Catalyst characterization

N_2 adsorption-desorption isotherms were collected at -196°C on a BELSORP-Max analyzer. Prior to each measurement, the catalyst was degassed under high vacuum at 300°C for 3 h. The surface area of each sample was obtained using the Brunauer-Emmett-Teller (BET) method and the pore size distribution was determined *via* the Barrett-Joyner-Halenda (BJH) method using desorption branch.

X-ray diffraction (XRD) patterns were measured on a SHIMADZU XRD-6100 Powder diffractometer using a Cu K α radiation source ($\lambda = 0.15406$ nm). The diffraction patterns were recorded over a 2θ range of 10 – 80° with a scan speed of 6° min^{-1} and a step size of 0.02° .

H_2 -temperature programmed reduction (H_2 -TPR) experiments were performed on a Quantachrome ChemBET Pulsar chemisorption analyzer with a thermal conductivity detector (TCD). H_2 -TPR curves were acquired in 5 vol% H_2/He from 50°C to 800°C with a temperature rate of $10^\circ\text{C min}^{-1}$ and held at 800°C for 30 min. Prior to each measurement, about 0.040 g sample was pretreated from room temperature to 500°C with a temperature rate of $10^\circ\text{C min}^{-1}$ in a flowing purified He gas (30 mL min^{-1}) and was then kept at 500°C for 30 min, in order to remove weakly adsorbed moisture and gas on the catalyst surface. After the sample was cooled to 50°C , the flowing gas was switched to 5 vol% $\text{H}_2 + \text{He}$ (30 mL min^{-1}) and the sample



was purged for 30 min until the TCD signal was stable. NH_3 -temperature programmed desorption (NH_3 -TPD) experiments were carried out using the same equipment. NH_3 -TPD curves were obtained in flowing He (30 mL min^{-1}) from 50°C to 800°C with a temperature ramp rate of $10^\circ\text{C min}^{-1}$, and 800°C was held for 30 min. The pretreatment procedure for NH_3 -TPD was similar to that of H_2 -TPR. Adsorption of NH_3 was conducted under flowing 5 vol% NH_3 + He for *ca.* 30 min at 100°C , and then purged with flowing He until the baseline became stable.

O_2 -TPD experiments were performed on a mass spectrometer (TILON GRP TECHNOLOGY LIMITED LC-D200M). O_2 -TPD curves were obtained under flowing N_2 (30 mL min^{-1}) from 100°C to 800°C with a temperature ramp rate of $10^\circ\text{C min}^{-1}$, and 800°C was held for 30 min. Prior to each measurement, about 100 mg of sample was pretreated in a U-shaped quartz tube at 500°C for 30 min under flowing N_2 (30 mL min^{-1}), followed by cooling to 100°C . Adsorption of oxygen was then conducted at 20 vol% O_2 + N_2 for *ca.* 30 min at 100°C until the O_2 signal became stable. After purging with flowing N_2 until the baseline signal reached a stable state, the O_2 -TPD signals began to be recorded with the mass-to-charge ratios ($m/z = 16$ and 32).

Transmission Electron Microscopy (TEM) was conducted on a Tecnai G2 F20 transmission electron microscope. More than 200 particles were randomly measured to determine the mean diameter of TiO_2 and $\text{MnO}_x/\text{TiO}_2$ catalysts, using the equation $d = \sum(n_i d_i) / \sum n_i$, where n_i is the number of particles with a diameter of d_i .

The components of the catalysts were examined on a Bruker S8 TIGERX X-Ray Fluorescence analyzer (XRF), equipped with a 60 kV X-ray tube (Rh K α radiation) with a maximum power of 4 W, and a maximum current of 170 mA. The XPS spectra were conducted on a Kratos Analytical AXIS Ultra DLD spectrometer with an Al K α radiation source ($h\nu = 1253.6 \text{ eV}$), operated at an accelerating power of 15 kW. The samples were degassed with vacuum-pumping to $5 \times 10^{-7} \text{ Pa}$ before the measurement. The binding energy was calibrated by the C 1s peak at 284.8 eV and the final spectra were obtained by subtracting a Shirley-type background.

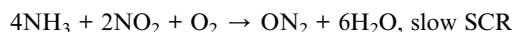
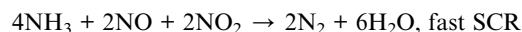
In situ diffusion reflection infrared Fourier transformed spectroscopy (DRIFTS) experiments were conducted on a Nicolet iS50 FTIR spectrometer equipped with a DRIFT cell containing ZnSe windows and MCT detector.³¹ The spectra were obtained from 4000 to 525 cm^{-1} at a resolution of 2 cm^{-1} by accumulating 32 scans. The temperature was controlled by a Pike temperature controller and the gas composition was governed by mass flow control (MFC). The catalyst was pretreated at 500°C for 1 h under flowing 20 vol% O_2 + N_2 (40 mL min^{-1}) and was then cooled down to 100°C . The background spectrum was recorded under flowing N_2 at 100°C , which was further subtracted from the sample spectrum.

3 Results and discussion

3.1 Catalytic performance

Fig. 1 shows the NH_3 -SCR catalytic performance of the $\text{MnO}_x/\text{TiO}_2(n)$ catalysts with various TiO_2 particle sizes. For all the catalysts, NO_x conversion firstly increased gradually from 65°C

to $265\text{--}290^\circ\text{C}$, and then decreased steadily with further increasing of the temperature to 400°C . The maximum NO_x conversion temperature was 265°C for $\text{MnO}_x/\text{TiO}_2(5\text{--}10)$, $\text{MnO}_x/\text{TiO}_2(10\text{--}25)$ and $\text{MnO}_x/\text{TiO}_2(40)$ and 290°C for $\text{MnO}_x/\text{TiO}_2(60)$. These results can be attributed to various SCR reaction pathways based on the NO_2/NO ratio.^{6,7,9,10,32} The pathway of the NH_3 -SCR reaction was regarded to occur *via* three reaction routes; namely, standard-, fast- and slow-SCR, which rest on the NO_2/NO fraction in the reaction feed.⁷



As shown in Fig. 1, at the initial stage, the reaction occurred through a standard route. With increasing reaction temperature, the NO_2/NO ratio increased through NO oxidation, inducing a variation in the main reaction pathway from the standard route to fast SCR. With increasing the reaction temperature, the ratio of NO_2/NO increased above 1, causing the main reaction pathway to change to slow SCR from fast SCR.^{33,34} By further increasing reaction temperature, the NO_2/NO ratio decreased with the restriction of the thermal equilibrium of NO_2 decomposition. The main reaction pathway changed to the standard SCR, thus decreasing the SCR catalytic activity.³³

In order to compare the catalytic performance of the various catalysts, T50 and T80 (the temperatures of NO_x conversion at 50% and 80%) were introduced and are shown in Fig. 1B. T50 decreased from 160°C to 155°C and 135°C , when the TiO_2 particle sizes decreased from 60 nm to 40 nm and 10–25 nm. Nevertheless, by further decreasing the TiO_2 particle size from 10–25 nm to 5–10 nm, T50 increased from 135°C to 185°C . A similar trend could be found in T80 as T50 over the corresponding catalysts. The catalytic activity of the $\text{MnO}_x/\text{TiO}_2(n)$ catalysts showed a volcano-type dependence on the TiO_2 particle size, reaching a maximum at 10–25 nm. These results illustrated that the SCR performance of the $\text{MnO}_x/\text{TiO}_2(n)$ catalysts varied with the TiO_2 support particle size. Soykal *et al.*³⁰ reported that the support particle size could change the reducibility and relative amount of redox sites on the catalyst surface. Generally, the SCR activity could be dependent on the surface acidity property, redox property and their synergistic effects.^{6,32} The various initial TiO_2 support sizes could affect the characteristics of the manganese oxide active sites, and could thereby have an impact on the SCR catalytic performance. Therefore, the characteristics of the supported manganese catalysts, such as redox, acidity and their synergistic effects, were then investigated to assess the effect of initial TiO_2 support particle size on the SCR performance of the $\text{MnO}_x/\text{TiO}_2(n)$ catalysts.

3.2 TEM

Fig. 2 shows TEM images of various TiO_2 support sizes. The size distribution of the various TiO_2 supports was $8.2 \pm 3.5 \text{ nm}$, $18.3 \pm 7.4 \text{ nm}$, $43.5 \pm 5.2 \text{ nm}$ and $63.6 \pm 5.2 \text{ nm}$, similar to as purchased. However, the size distributions of the various $\text{MnO}_x/$



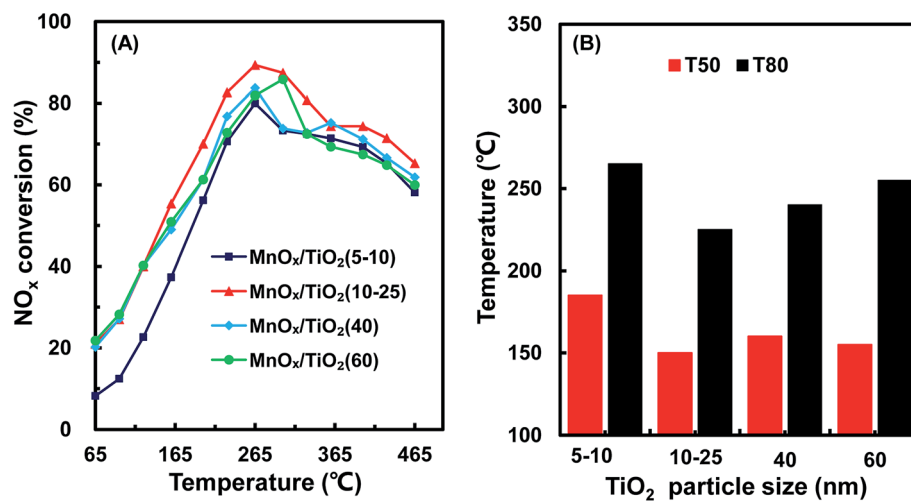


Fig. 1 NO_x conversion (A), T50 and T80 (B) of MnO_x/TiO₂(*n*) with various TiO₂ particle sizes.

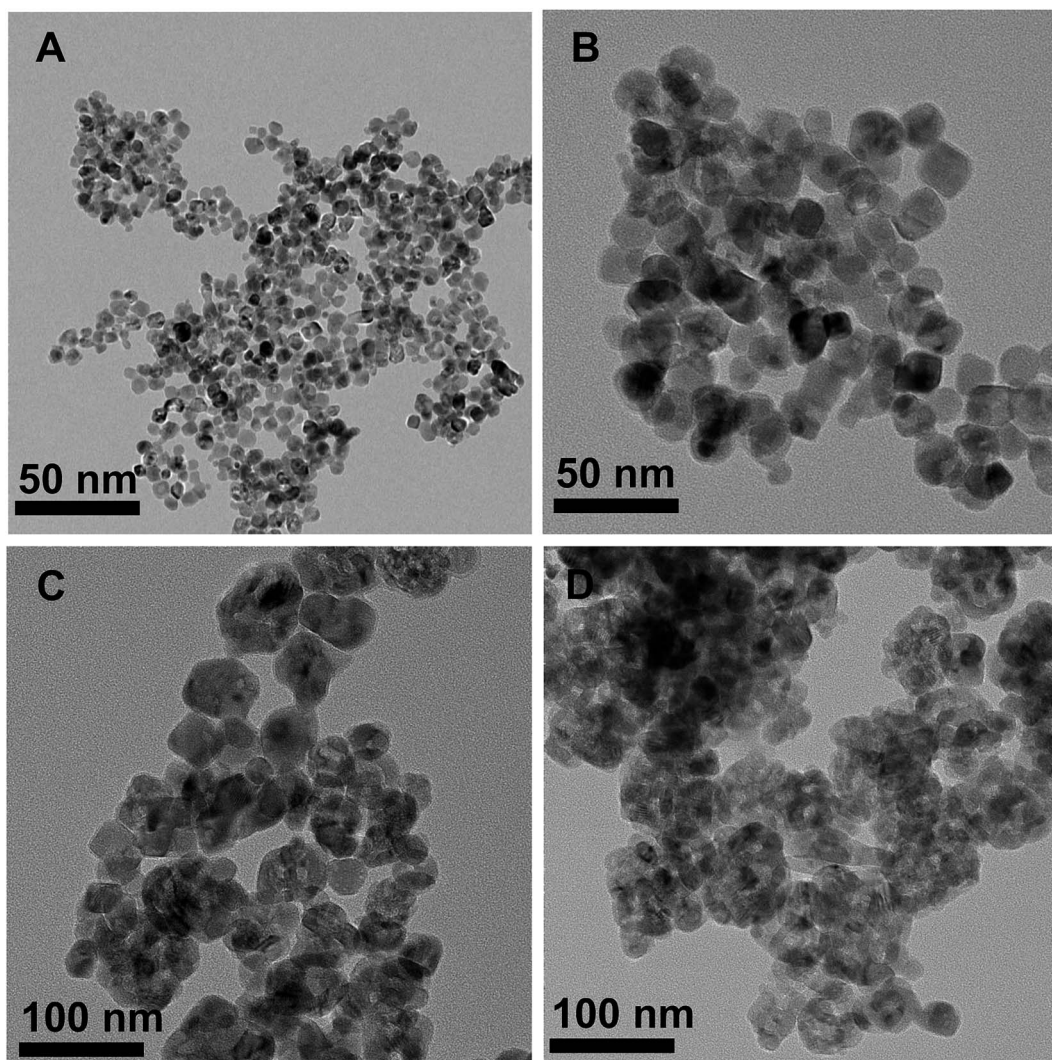


Fig. 2 TEM images of the various TiO₂(*n*) supports of *n* = 5–10 (A), 10–25 (B), 40 (C) and 60 (D).

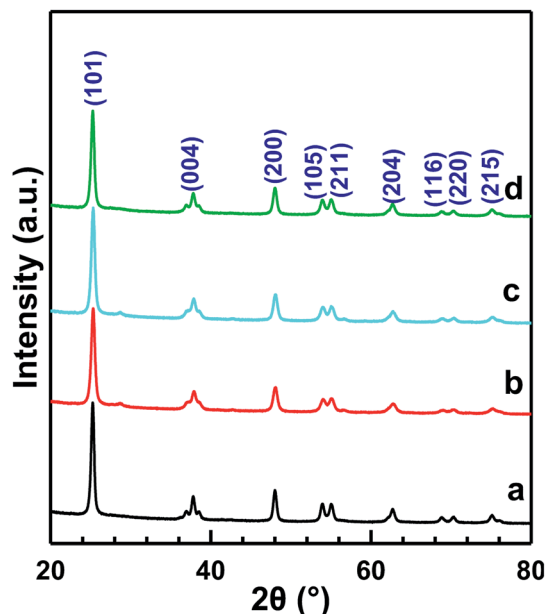


Fig. 3 XRD patterns of $\text{MnO}_x/\text{TiO}_2(n)$ catalysts: $n = 5-10$ (a), $10-25$ (b), 40 (c) and 60 (d).

TiO_2 catalysts, as shown in Fig. S1,[†] were similar. All the $\text{MnO}_x/\text{TiO}_2$ catalysts had an average diameter of *ca.* 55 nm. These results revealed that the impregnation and calcination process resulted in the variation in the particle sizes of the $\text{MnO}_x/\text{TiO}_2$ catalysts.

3.3 XRD

Fig. 3 shows the XRD patterns of $\text{MnO}_x/\text{TiO}_2(n)$ with various TiO_2 particle sizes. All of the catalysts showed the same 2θ diffraction positions and different diffraction intensities. The diffraction of 2θ at 25.3° , 37.8° , 48.0° , 53.9° , 55.1° , 62.8° , 68.9° , 70.5° and 75.2° could be assigned to (101), (004), (200), (105), (211), (204), (116), (220) and (215) planes of anatase- TiO_2

(JCPDS, 65-5714), respectively. The theoretical monolayer coverage amount could be estimated from structural calculations.³⁵⁻³⁷ Based on the cation density of MnO_x , a reference value of 15 \AA^2 per MnO_x unit was used to calculate the monolayer surface coverage.³⁵⁻³⁷ The virtual loading was *ca.* 3.1 wt% Mn for monolayer surface coverage, according to the surface area of our investigated samples. Mn loading in our investigated catalysts was 10 wt%, which was more than three times that of the monolayer manganese amount. However, no independent diffraction peaks corresponding to manganese oxides could be observed in all the samples, indicating that the incorporated manganese oxides were in a highly dispersed state or in an amorphous or poorly crystalline state. These results could be ascribed to the strong interaction between Mn and anatase TiO_2 , which is in agreement with the previous reports.^{20,23}

3.4 Textural properties of the catalysts

Fig. 4 shows the N_2 adsorption/desorption isotherms and pore size distributions of the $\text{MnO}_x/\text{TiO}_2(n)$ catalysts with various TiO_2 particle sizes. For all the $\text{MnO}_x/\text{TiO}_2(n)$ catalysts, the N_2 adsorption/desorption isotherms show similar type IV behavior and hysteresis loops attributed to type H1. The corresponding quantification parameters of the textural properties, including BET specific surface area, total pore volume and average pore diameter, are shown in Table 1. All of the catalysts showed similar specific surface areas ($50.2-57.4 \text{ m}^2 \text{ g}^{-1}$), pore volumes ($0.27-0.29 \text{ mL g}^{-1}$) and mean pore diameters (20–27 nm). It should be noted that the pore sizes were much larger than the dynamic size of the feed gas, indicating that the pore structures of the $\text{MnO}_x/\text{TiO}_2(n)$ catalysts were feasible for reactant molecule diffusion.

3.5 H_2 -TPR

The redox properties of catalysts play an important role in the NH_3 -SCR reaction. Thus, H_2 -TPR experiments were carried out

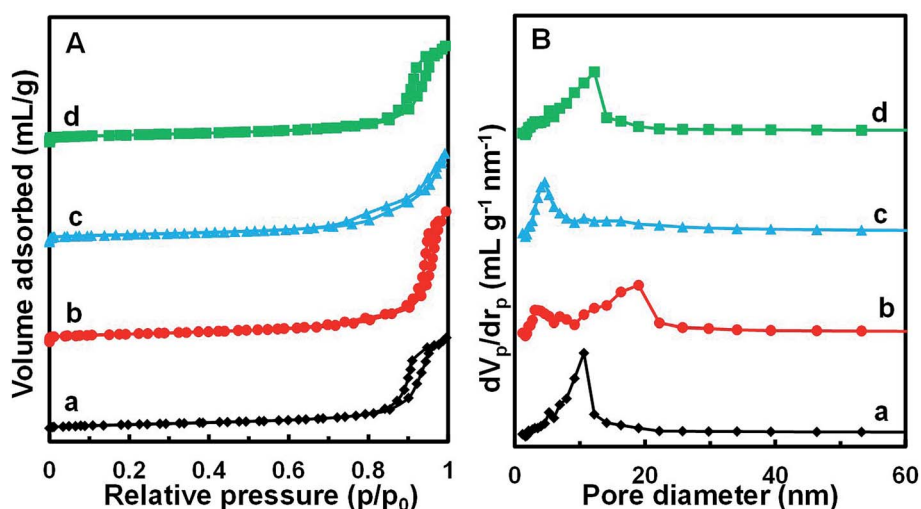


Fig. 4 N_2 adsorption/desorption isotherms (A) and BJH pore distribution curves (B) of $\text{MnO}_x/\text{TiO}_2(n)$ catalysts: $n = 5-10$ (a), $10-25$ (b), 40 (c) and 60 (d).



Table 1 BET specific surface area, total pore volume, mean pore diameter surface composition of $\text{MnO}_x/\text{TiO}_2(n)$ catalysts with various TiO_2 support particle sizes

Catalyst	BET surface area ($\text{m}^2 \text{g}^{-1}$)	Pore volume (mL g^{-1})	Average pore diameter (nm)	$\text{Mn}^{4+}/\text{Mn}_{\text{total}}^a$
$\text{MnO}_x/\text{TiO}_2(5-10)$	51.5	0.29	22.2	0.29
$\text{MnO}_x/\text{TiO}_2(10-25)$	57.4	0.29	27.2	0.48
$\text{MnO}_x/\text{TiO}_2(40)$	54.0	0.27	19.8	0.35
$\text{MnO}_x/\text{TiO}_2(60)$	50.2	0.29	23.4	0.34

^a Determined by XPS.

to determine the oxidative properties of the $\text{MnO}_x/\text{TiO}_2(n)$ catalysts and the results are shown in Fig. 5. All of the catalysts exhibited two broad hydrogen consumption peaks. The lower temperature reduction peak in the temperature range of 300–450 °C could be attributed to the reduction of Mn^{4+} to Mn^{3+} and Ti^{4+} to Ti^{3+} , which originated from interaction between MnO_x and TiO_2 .^{23,38–41} The higher temperature peak in the temperature range of 450–600 °C could be ascribed to the reduction of Mn^{3+} to Mn^{2+} .^{38,42,43} It should be noted that the temperature peaks were different for $\text{MnO}_x/\text{TiO}_2(n)$ with different initial TiO_2 particle sizes. For $\text{MnO}_x/\text{TiO}_2(5-10)$, $\text{MnO}_x/\text{TiO}_2(10-25)$, $\text{MnO}_x/\text{TiO}_2(40)$ and $\text{MnO}_x/\text{TiO}_2(60)$, the reduction peaks at lower temperature were centered at 400 °C, 364 °C, 384 °C and 367 °C, while the higher temperature reduction peaks were 525 °C, 516 °C, 527 °C and 521 °C, respectively. In previous studies, the SCR performance of $\text{MnO}_x/\text{TiO}_2$ catalysts has been related to the oxidation state of surface Mn atoms, especially the properties of surface Mn^{4+} species.^{38,42,43} The lower peak temperature of $\text{MnO}_x/\text{TiO}_2(n)$ represents a higher oxidative property and oxygen mobility. The order of the peak temperatures in the temperature

range of 300–450 °C for the $\text{MnO}_x/\text{TiO}_2(n)$ catalysts was as follows: $\text{MnO}_x/\text{TiO}_2(10-25)$ (364 °C) < $\text{MnO}_x/\text{TiO}_2(60)$ (367 °C) < $\text{MnO}_x/\text{TiO}_2(40)$ (384 °C) < $\text{MnO}_x/\text{TiO}_2(5-10)$ (400 °C). $\text{MnO}_x/\text{TiO}_2(60)$ and $\text{MnO}_x/\text{TiO}_2(40)$ showed different trends in their corresponding SCR catalytic activity. The catalytic activity was not only decided by the properties of active sites, but also relied on the number of active sites. The peak area in the temperature range of 300–450 °C for $\text{MnO}_x/\text{TiO}_2(40)$, which was associated with the amount of Mn^{4+} , was higher than that for $\text{MnO}_x/\text{TiO}_2(60)$. Therefore, the properties and amount of Mn^{4+} in $\text{MnO}_x/\text{TiO}_2(n)$ could also be affected by the TiO_2 particle size, thus influencing the SCR catalytic activity.

3.6 O_2 -TPD

In order to further confirm the oxidative properties and oxygen mobility, O_2 -TPD was then used to characterize the oxygen mobility of the $\text{MnO}_x/\text{TiO}_2(n)$ catalysts. Fig. 6 shows the O_2 -TPD curves of the $\text{MnO}_x/\text{TiO}_2(n)$ catalysts with various TiO_2 particle sizes. For all of the $\text{MnO}_x/\text{TiO}_2(n)$ catalysts, there are two desorption peaks centered at 500–700 °C and 700–800 °C, respectively. The desorption of O_2 at a temperature above 200 °C in O_2 -TPD for the manganese-based catalysts is associated with the evolution of oxygen from the lattice (surface or bulk).⁴⁴ The lower temperature peak in the temperature range of 500–700 °C was attributed to the surface lattice oxygen and related to the surface oxygen vacancies, which is often correlated with a high oxidation ability.^{45,46} The higher temperature peak at temperatures above 700 °C could be assigned to bulk lattice oxygen, which was generally not correlated to oxidation ability and strongly bound to the lattice.⁴⁶ The peak temperature in the temperature range of 500–700 °C for $\text{MnO}_x/\text{TiO}_2(10-25)$ was 560 °C, which was lower than that of $\text{MnO}_x/\text{TiO}_2(5-10)$ (630 °C), $\text{MnO}_x/\text{TiO}_2(40)$ (621 °C) and $\text{MnO}_x/\text{TiO}_2(60)$ (586 °C). Meanwhile, the order of the lower temperature peak amount was similar to H_2 -TPR.

3.7 NH_3 -TPD

The surface acid sites of the catalysts played a significant role in the NH_3 -SCR reaction, which could adsorb and activate NH_3 . NH_3 -TPD was used to study the surface acidity of $\text{MnO}_x/\text{TiO}_2(n)$, as depicted in Fig. 7. For all the $\text{MnO}_x/\text{TiO}_2(n)$ catalysts, the NH_3 -TPD curves featured a broad peak between 100 and 400 °C. All these desorption peaks were divided into two or three peaks based on the Gaussian peak shape model. The desorption peaks

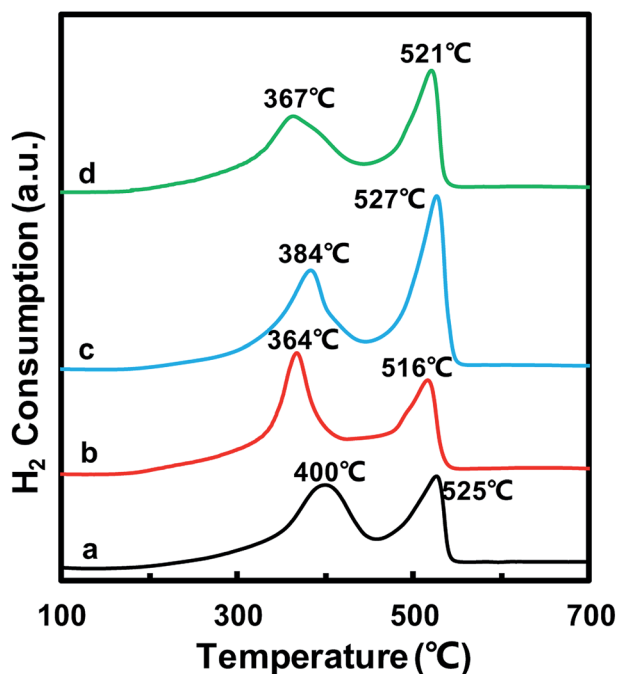


Fig. 5 H_2 -TPR profiles of the $\text{MnO}_x/\text{TiO}_2(n)$ catalysts: $n = 5-10$ (a), $10-25$ (b), 40 (c) and 60 (d).



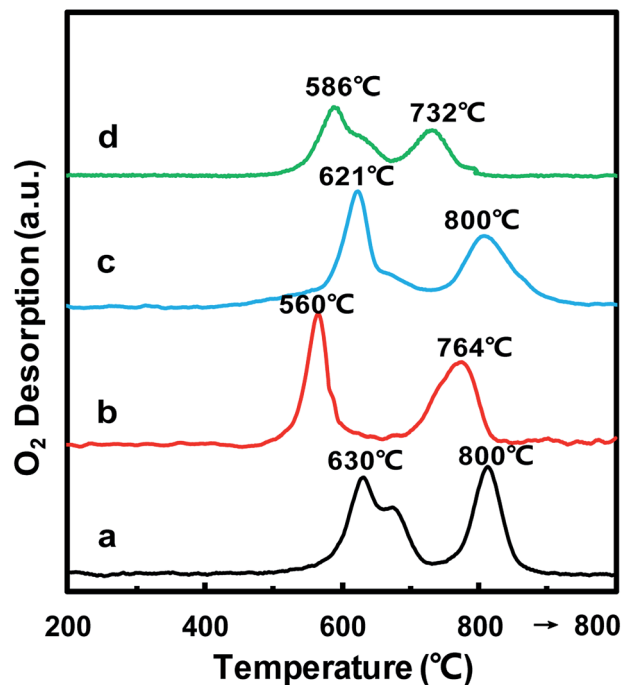


Fig. 6 O_2 -TPD profiles of $MnO_x/TiO_2(n)$ catalysts of $n = 5-10$ (a), $10-25$ (b), 40 (c) and 60 (d).

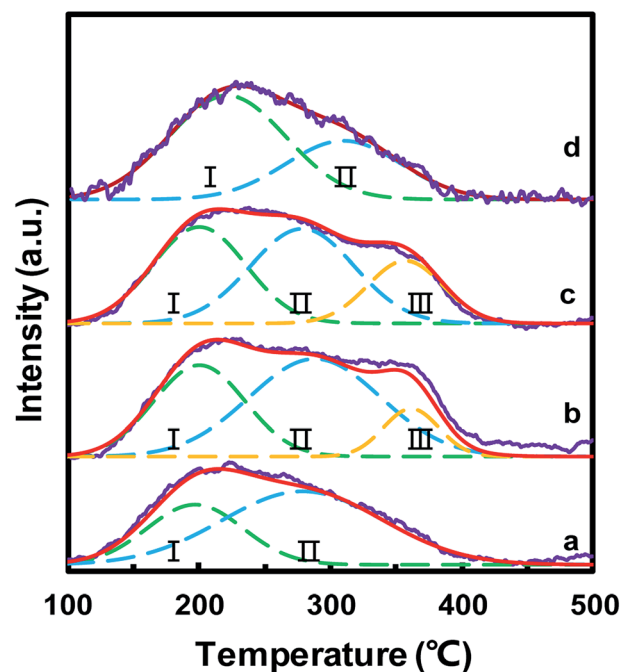


Fig. 7 NH_3 -TPD profiles of the $MnO_x/TiO_2(n)$ catalysts: $n = 5-10$ (a), $10-25$ (b), 40 (c) and 60 (d).

were labeled as I, II and III, according to the peak temperature from low to high, which could be attributed to the NH_3 desorbed from weak acid sites, medium acid sites and strong acid sites, respectively.^{17,47} The peak temperature and corresponding area in NH_3 -TPD were calculated and are listed in Table 2. The peak temperature of MnO_x/TiO_2 with $TiO_2 < 40$ nm was *ca.*

Table 2 Quantitative analysis of NH_3 -TPD for the $MnO_x/TiO_2(n)$ catalysts

Catalyst	Temperature ($^{\circ}C$)			Acid amount ($\mu mol\ g^{-1}$)			
	T_I	T_{II}	T_{III}	S_I	S_{II}	S_{III}	$S_I + S_{II} + S_{III}$
$Mn/TiO_2(5-10)$	197	279	—	194	397	—	591
$Mn/TiO_2(10-25)$	200	288	361	279	430	89	798
$Mn/TiO_2(40)$	200	279	357	301	329	158	789
$Mn/TiO_2(60)$	222	310	—	408	228	—	636

$200\ ^{\circ}C$, which is lower than that of $MnO_x/TiO_2(60)$. More importantly, the order of the acid amount for the $MnO_x/TiO_2(n)$ catalysts was as follows: $MnO_x/TiO_2(10-25) > MnO_x/TiO_2(40) > MnO_x/TiO_2(60) > MnO_x/TiO_2(5-10)$, which is also in accordance with the catalytic activity of the counterpart catalysts, suggesting that the particle size of the support not only influences the oxidizing ability but also the acidic properties.

Compared with larger TiO_2 support particle size, a smaller TiO_2 particle size could provide a greater boundary area between active sites and supports, which is beneficial for the synergistic effect between acid sites and redox sites. As previously reported, low-temperature selective catalytic reduction mainly occurs *via* a Langmuir-Hinshelwood mechanism. The SCR activity was controlled not only by the activation of NO , O_2 and NH_3 reactant, but also by the synergistic effect between acid sites and redox sites.

3.8 XPS

In order to further acquire information regarding the oxidation state of manganese on the catalyst surface, XPS spectra of the $MnO_x/TiO_2(n)$ catalysts were recorded. Fig. 8 shows the Mn 2p spectra of the MnO_x/TiO_2 catalysts with various TiO_2 particle sizes. The Mn 2p spectra of $MnO_x/TiO_2(n)$ catalysts were deconvoluted based on the Gaussian-Lorentzian (GL(30)) line shape after subtracting a Shirley baseline. All the Mn $2p_{1/2}$ and $2p_{3/2}$ peaks of each Mn species have the same half height peak width and the center of the Mn $2p_{1/2}$ and $2p_{3/2}$ peaks was 11.7 eV. Mn 2p spectra of the $MnO_x/TiO_2(n)$ catalysts could be divided into two peaks with maxima at 644.1–645.3 eV and 641.9–642.5 eV, which can be assigned to Mn^{4+} and Mn^{3+} , respectively.^{23,41,42,48,49} The quantitation results of the Mn^{4+}/Mn molar ratio in XPS spectra are shown in Table 1. It can be seen that the Mn^{4+}/Mn molar ratio of the $MnO_x/TiO_2(10-25)$ catalyst was 0.48, which is higher than 0.35 for $MnO_x/TiO_2(40)$, 0.34 for $MnO_x/TiO_2(60)$ and 0.29 for $MnO_x/TiO_2(5-10)$. Moreover, the order of the surface Mn^{4+}/Mn molar ratio on the $MnO_x/TiO_2(n)$ catalysts was as follows: $MnO_x/TiO_2(10-25) > MnO_x/TiO_2(40) > MnO_x/TiO_2(60) > MnO_x/TiO_2(5-10)$, which agrees well with the SCR catalytic performance. These results demonstrate that the TiO_2 particle size could influence the oxidation state of surface manganese oxides, leading to the variation in Mn^{4+} concentration, which could be ascribed to the interaction between manganese oxides and titanium.^{42,50} Thirupathi *et al.* also investigated the effect of the surface manganese species on the SCR performance and found that surface Mn^{4+} on the TiO_2



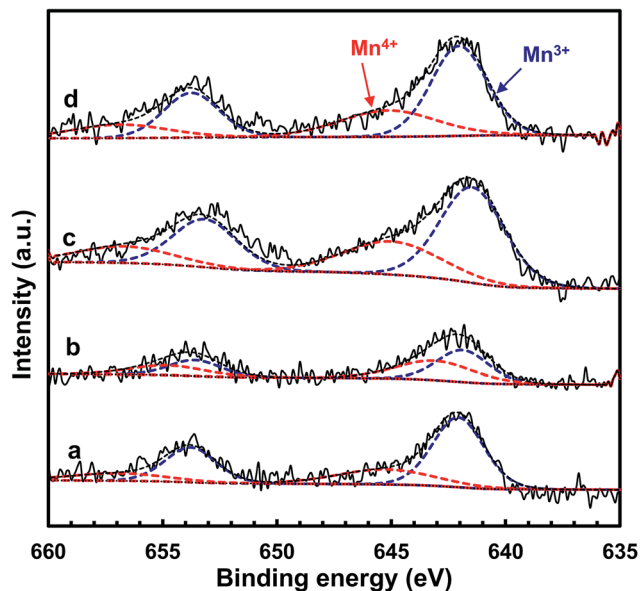


Fig. 8 XPS spectra for Mn 2p of the $\text{MnO}_x/\text{TiO}_2(n)$ catalysts: $n = 5-10$ (a), $10-25$ (b), 40 (c) and 60 (d).

support was directly associated with the SCR performance.⁴² All of these results revealed that initial TiO_2 particle size can affect the oxidizing ability and oxygen mobility. The higher oxidizing ability could increase the NO_2/NO_x ratio in the actual reaction feed, which could increase the proportion of “fast SCR” reaction route, and thereby enhance the SCR activity.⁵⁰

3.9 In situ DRIFTS studies

3.9.1 $\text{NO} + \text{O}_2$ adsorption. In order to understand the mechanism of the $\text{MnO}_x/\text{TiO}_2(n)$ catalysts, DRIFT spectra of $\text{MnO}_x/\text{TiO}_2(10-25)$ were studied. Fig. 9 shows the DRIFT spectra of $\text{NO} + \text{O}_2$ adsorption over $\text{MnO}_x/\text{TiO}_2(10-25)$ for various times at 100°C . Bands at 1607 , 1580 , 1492 , 1446 , 1300 , 1282 and 1257 cm^{-1} were detected. The band at 1607 cm^{-1} could be ascribed to the bridge nitrate.⁵⁰⁻⁵³ The bands at 1580 , 1300 and 1282 cm^{-1} could be assigned to bidentate nitrate.^{41,51-54} The bands at 1492 and 1257 cm^{-1} could be identified as monodentate nitrate.^{52,55} The wide peak in the region of $1430-1550\text{ cm}^{-1}$ could be attributed to the bidentate nitrate on the surface of the sample.^{52,55} The band at 1446 cm^{-1} was assigned to nitro compounds.⁵⁴ In the first 5 min, only bridge nitrate (band at 1607 cm^{-1}) and bidentate nitrate (bands at 1580 , 1300 and 1282 cm^{-1}) were detected on the manganese oxides. With increasing time, monodentate nitrate (bands at 1492 and 1257 cm^{-1}) on the manganese oxides appeared. Meanwhile, bidentate nitrate on the surface of the sample (the wide peak in the region of $1430-1550\text{ cm}^{-1}$) increased with exposure time. These results illustrated that NO_x first adsorbed on manganese oxides as bridge and bidentate nitrate, and then as monodentate nitrate.

3.9.2 NH_3 adsorption after $\text{NO} + \text{O}_2$ adsorption. To understand the role of various adsorbed NO_x species during the NH_3 -SCR reaction, the *in situ* DRIFT spectra for the pre-adsorbed $\text{NO} + \text{O}_2$ and NH_3 at 100°C as a function of time

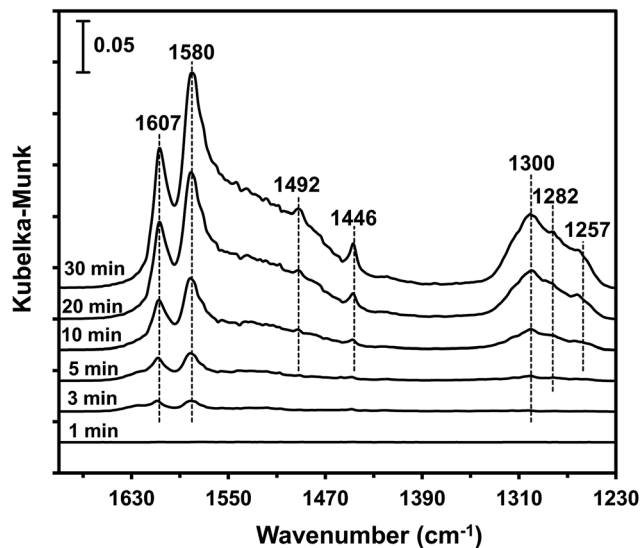


Fig. 9 DRIFT spectra of $\text{MnO}_x/\text{TiO}_2(10-25)$ exposed to $500\text{ ppm NO} + 5\% \text{ O}_2 + \text{N}_2$ at 100°C for various times.

are shown in Fig. 10. A reaction temperature of 100°C was chosen to decrease the reaction rate; therefore the surface species on the catalyst surface could be enhanced to a detectable level.⁵⁶ When 500 ppm NH_3 was introduced to the catalyst pretreated by $\text{NO} + \text{O}_2$, the intensity of the band at 1607 cm^{-1} assigned to bridge nitrate on manganese oxides decreased immediately with the increase of time. Meanwhile, the intensity of the bands at 1580 and 1295 cm^{-1} (shown in Fig. 10C) assigned to bidentate nitrate on the manganese oxides decreased gradually. However, the variation of the intensity of the band at 1257 cm^{-1} assigned to monodentate nitrate on the manganese oxides was different, and remained constant, indicating that the monodentate nitrate was not contributing to the SCR reaction at 100°C . Simultaneously, the intensity of the bands at 3341 and 3244 cm^{-1} (shown in Fig. 10D) assigned to asymmetric stretching and symmetric stretching of NH_3 coordinated to Lewis acid sites, increased immediately with the addition of NH_3 .^{51,57,58} It is reasonable to assume that the band at 1598 cm^{-1} assigned to coordinated NH_3 on Lewis acid sites was caused by the overlap of the bridge and bidentate nitrates in the regions of 1630 and 1550 cm^{-1} . These results indicated that bridge and bidentate nitrates were the main contributors to the low-temperature SCR reaction, fitting the Langmuir-Hinshelwood mechanism suggested in previous works.^{55,57,59,60} It should be noted that the band due to the bridge and bidentate nitrates did not completely vanish, even when the NH_3 purging time was prolonged to 60 min , suggesting that NO_x species adsorbed on various manganese species showed different SCR activity. More importantly, the band (shown in Fig. 10B) assigned to bridge nitrate shifted from 1607 cm^{-1} to 1600 cm^{-1} , illustrating that adsorbed NO_x species at higher wavenumbers in the IR band showed superior SCR activity, since the IR band position was statistically evaluated according to the similar structures of the various surface manganese species. Based on our previous characterization results, such as those from H_2 -TPR, O_2 -TPD and XPS, the surface valence states of manganese with various



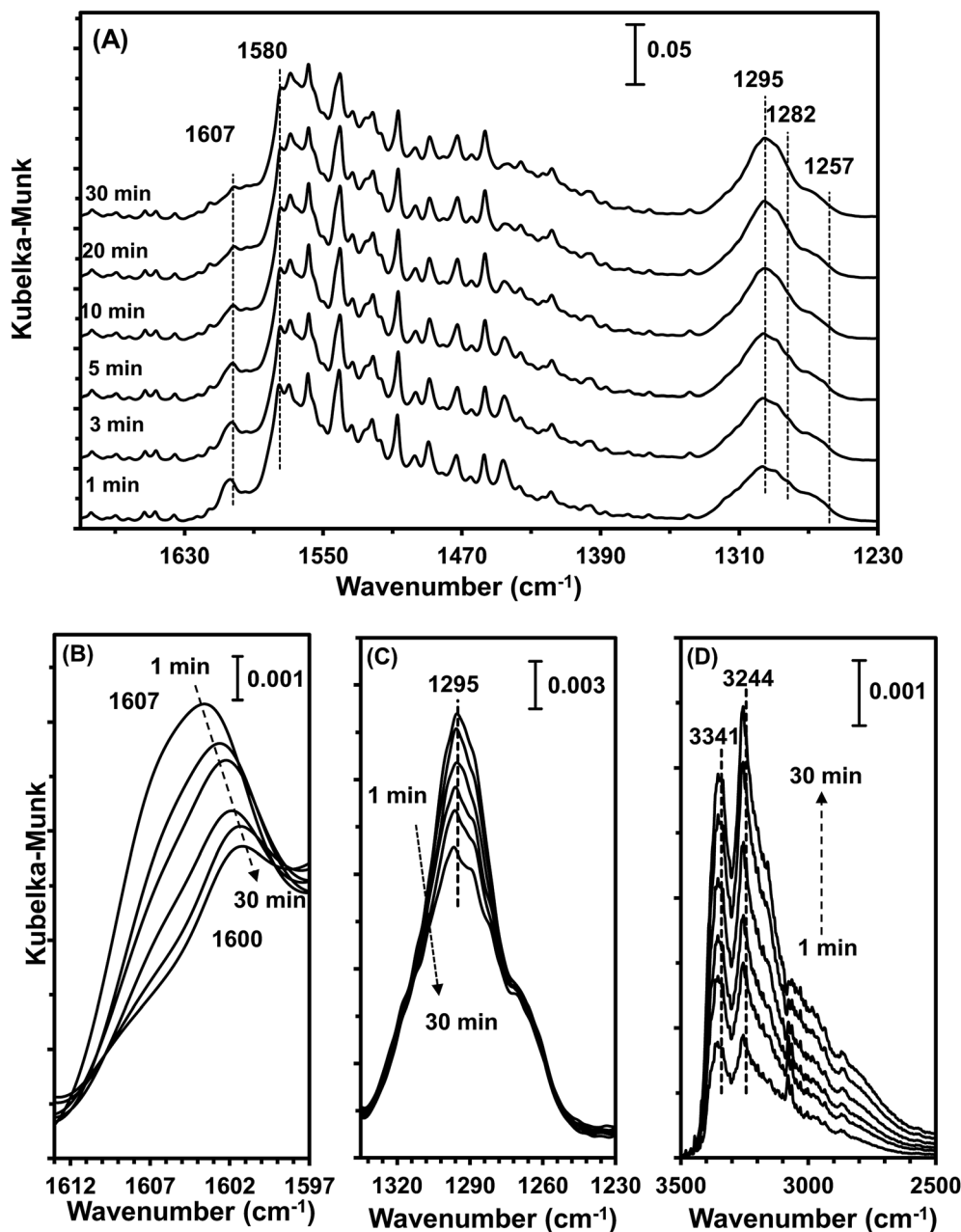


Fig. 10 DRIFT spectra of $\text{MnO}_x/\text{TiO}_2(10-25)$ pretreated by exposure to 500 ppm $\text{NO} + 5\% \text{O}_2 + \text{N}_2$ followed by exposure to 500 ppm $\text{NH}_3 + \text{N}_2$ at 100°C for various times.

initial support sizes contained different compositions of Mn^{4+} and Mn^{3+} . The IR vibration frequencies in the N–O stretching modes could be varied *via* the formation of π -back bands.⁶¹ With high-valent cations (Mn^{4+}), which are poor in d-electrons, the extent of π -back donation is lower than that in low-valent cations (Mn^{3+}), thus increasing the vibration frequency or wavenumber. The bridge nitrate at a higher wavenumber could be attributed to the NO_x adsorbed on the high-valent manganese species, Mn^{4+} . Based on the previous DRIFTS results, the higher wavenumber IR band (1607 cm^{-1}) decreased more quickly than the lower one. Therefore, we deduced that NO_x

adsorbed species on Mn^{4+} was the dominant factor influencing the low-temperature SCR activity.

3.9.3 $\text{NO} + \text{O}_2$ adsorption after NH_3 adsorption. Furthermore, in order to understand the function of adsorbed NH_3 species during the NH_3 -SCR reaction, DRIFT spectra of $\text{MnO}_x/\text{TiO}_2(10-25)$ in a flow of $\text{NO} + \text{O}_2$ were collected, after the catalyst was pre-exposed to a NH_3 for 60 min followed by N_2 purging for 30 min at 100°C , as shown in Fig. S2.† The intensity of the bands at 3410 and 3244 cm^{-1} assigned to NH stretching remained unchanged, illustrating that the low-temperature SCR reaction did not occur *via* an Eley–Rideal mechanism but *via*



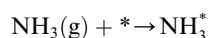
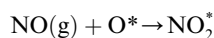
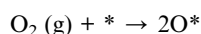
a Langmuir–Hinshelwood mechanism, which coincides with previous work.⁶

3.10 Origin of SCR activity

Combining the results obtained in this study, we could conclude that the low-temperature SCR activity over MnO_x/TiO₂ occurred *via* a Langmuir–Hinshelwood mechanism.

Therefore, the NH₃-SCR reaction over MnO_x/TiO₂ can be described by the following pathways.

At low temperature, the reaction pathway occurred as a Langmuir–Hinshelwood mechanism.⁶



The type of adsorbed NO_x species on manganese oxides has a prominent effect on the SCR activity. The order of SCR activity of various adsorbed nitrates was as follows: bridge nitrate > bidentate nitrate > monodentate nitrate. The bridge nitrate and bidentate nitrate were the main contributors to the SCR activity, while the monodentate nitrate showed no activity, which agreed with previous work.⁵⁰ Moreover, among all the bridge nitrates on various manganese oxides, bridge nitrate on the high-valence manganese species (*e.g.* Mn⁴⁺) was the most active species in the low-temperature SCR reaction, which could be proved by the blue shift on the DRIFT spectra in a flow of NH₃ after pretreatment with NO + O₂. A higher Mn⁴⁺/Mn molar ratio could produce more bridge nitrate on Mn⁴⁺, thus increasing the SCR activity.

4 Conclusions

In this work, a series of MnO_x/TiO₂ catalysts with various initial TiO₂ particle sizes was prepared *via* an impregnation method for the selective catalytic reduction of NO with NH₃. The MnO_x/TiO₂(10–25) catalyst showed superior low-temperature SCR catalytic activity. The XRD results illustrated a high dispersion of manganese oxides on all the catalysts *via* interactions between manganese oxides and anatase TiO₂. H₂-TPR, O₂-TPD, NH₃-TPD and XPS results indicated that the acid amount and Mn⁴⁺/Mn molar ratio were dependent on the initial TiO₂ support particle size. The order of surface acidity and Mn⁴⁺/Mn molar ratio was as follows: MnO_x/TiO₂(10–25) > MnO_x/TiO₂(40) > MnO_x/TiO₂(60) > MnO_x/TiO₂(5–10), which agreed well with the order of SCR activity on the corresponding catalysts. Furthermore, the *in situ* DRIFTS results showed that the low-temperature SCR reaction occurred *via* a Langmuir–Hinshelwood mechanism and the adsorbed NO_x was the key factor in

the low-temperature SCR activity. The order of adsorbed NO_x species activity on manganese oxides was as follows: bridge nitrate > bidentate nitrate > monodentate nitrate. Moreover, the bridge nitrate on Mn⁴⁺ was the greatest contributor to the low-temperature SCR activity. The variation of the initial TiO₂ support particle size influenced the surface Mn⁴⁺/Mn molar ratio of the MnO_x/TiO₂ catalysts, which would promote the reactivity of the bridge nitrate, therefore enhancing SCR performance.

Conflicts of interest

There are no conflicts to declare.

Acknowledgements

We acknowledge the financial support from the China Post-doctoral Science Foundation (2017M613143), the Natural Science Foundation of Shaanxi Province of China (2017JQ2016), and the National Natural Science Foundation of China (21802107).

References

- 1 X. Liu, Y. Zhang, W. Han, A. Tang, J. Shen, Z. Cui, P. Vitousek, J. W. Erisman, K. Goulding, P. Christie, A. Fangmeier and F. Zhang, *Nature*, 2013, **494**, 459–462.
- 2 Y. Cheng, G. Zheng, C. Wei, Q. Mu, B. Zheng, Z. Wang, M. Gao, Q. Zhang, K. He, G. Carmichael, U. Poschl and H. Su, *Sci. Adv.*, 2016, **2**, e160153012.
- 3 S. Roy and A. Baiker, *Chem. Rev.*, 2009, **109**, 4054–4091.
- 4 Z. Hu, K. Q. Sun, W. Z. Li and B.-Q. Xu, *Catal. Today*, 2010, **158**, 432–438.
- 5 Z. Hu, W.-Z. Li, K.-Q. Sun and B.-Q. Xu, *Catal. Sci. Technol.*, 2013, **3**, 2062–2071.
- 6 C. Liu, J. Shi, C. Gao and C. Niu, *Appl. Catal., A*, 2016, **522**, 54–69.
- 7 R. Zhang, N. Liu, Z. Lei and B. Chen, *Chem. Rev.*, 2016, **116**, 3658–3721.
- 8 J. Wang, H. Zhao, G. Haller and Y. Li, *Appl. Catal., B*, 2017, **202**, 346–354.
- 9 W. Shan and H. Song, *Catal. Sci. Technol.*, 2015, **5**, 4280–4288.
- 10 Z. Liu, J. Li and S. I. Woo, *Energy Environ. Sci.*, 2012, **5**, 8799–8814.
- 11 F. Liu, W. Shan, D. Pan, T. Li and H. He, *Chin. J. Catal.*, 2014, **35**, 1438–1445.
- 12 A. M. Beale, F. Gao, I. Lezcano-Gonzalez, C. H. F. Peden and J. Szanyi, *Chem. Soc. Rev.*, 2015, **44**, 7371–7405.
- 13 X. Hu, L. Huang, J. Zhang, H. Li, K. Zha, L. Shi and D. Zhang, *J. Mater. Chem. A*, 2018, **6**, 2952–2963.
- 14 K. Zha, L. Kang, C. Feng, L. Han, H. Li, T. Yan, P. Maitrad, L. Shi and D. Zhang, *Environ. Sci.: Nano*, 2018, **5**, 1408–1419.
- 15 K. Zha, S. Cai, H. Hu, H. Li, T. Yan, L. Shi and D. Zhang, *J. Phys. Chem. C*, 2017, **121**, 25243–25254.
- 16 C. Li, X. Tang, H. Yi, L. Wang, X. Cui, C. Chu, J. Li, R. Zhang and Q. Yu, *Appl. Surf. Sci.*, 2018, **428**, 924–932.



- 17 Z. Fan, J. Shi, C. Gao, G. Gao, B. Wang and C. Niu, *ACS Appl. Mater. Interfaces*, 2017, **9**, 16117–16127.
- 18 L. Yan, Y. Liu, K. Zha, H. Li, L. Shi and D. Zhang, *ACS Appl. Mater. Interfaces*, 2017, **9**, 2581–2593.
- 19 P. G. Smirniotis, D. A. Pena and B. S. Uphade, *Angew. Chem., Int. Ed.*, 2001, **40**, 2479–2482.
- 20 P. G. Smirniotis, P. M. Sreekanth, D. A. Peña and R. G. Jenkins, *Ind. Eng. Chem. Res.*, 2006, **45**, 6436–6443.
- 21 Y. J. Kim, H. J. Kwon, I. Nam, J. W. Choung, J. K. Kil, H. Kim, M. Cha and G. K. Yeo, *Catal. Today*, 2010, **151**, 244–250.
- 22 J. Li, J. Chen, R. Ke, C. Luo and J. Hao, *Catal. Commun.*, 2007, **8**, 1896–1900.
- 23 P. R. Ettireddy, N. Ettireddy, S. Mamedov, P. Boolchand and P. G. Smirniotis, *Appl. Catal., B*, 2007, **76**, 123–134.
- 24 S. Yang, F. Qi, S. Xiong, H. Dang, Y. Liao, P. K. Wong and J. Li, *Appl. Catal., B*, 2016, **181**, 570–580.
- 25 B. Xu, J. Wei, Y. Yu, J. Li and Q. Zhu, *Top. Catal.*, 2003, **22**, 77–85.
- 26 B. Xu, J. Wei, Y. Yu, Y. Li, J. Li and Q. Zhu, *J. Phys. Chem. B*, 2003, **107**, 5203–5207.
- 27 Q. Zhang, Y. Li and B. Xu, *Catal. Today*, 2004, **98**, 601–605.
- 28 M. M. Pakulska, C. M. Grgicak and J. B. Giorgi, *Appl. Catal., A*, 2007, **332**, 124–129.
- 29 M. Murdoch, G. I. N. Waterhouse, M. A. Nadeem, J. B. Metson, M. A. Keane, R. F. Howe, J. Llorca and H. Idriss, *Nat. Chem.*, 2011, **3**, 489–492.
- 30 I. I. Soykal, H. Sohn and U. S. Ozkan, *ACS Catal.*, 2012, **2**, 2335–2348.
- 31 Z. Hu, S. Tan, R. Mi, X. Li, D. Li and B. Yang, *Catal. Lett.*, 2018, **148**, 1490–1498.
- 32 J. Li, H. Chang, L. Ma, J. Hao and R. T. Yang, *Catal. Today*, 2011, **175**, 147–156.
- 33 M. Koebel, G. Madia and M. Elsener, *Catal. Today*, 2002, **73**, 239–247.
- 34 M. Devadas, O. Krocher, M. Elsener, A. Wokaun, N. Söger, M. Pfeifer, Y. Demel and L. Mussmann, *Appl. Catal., B*, 2006, **67**, 187–196.
- 35 E. F. Massoth, *Adv. Catal.*, 1978, **2**, 265–310.
- 36 G. C. Bond and S. F. Tahir, *Appl. Catal.*, 1991, **71**, 1–31.
- 37 J. M. Gallardo-Amores, T. Armaroli, G. Ramis, E. Finocchio and G. Busca, *Appl. Catal., B*, 1999, **22**, 249–259.
- 38 E. Park, S. Chin, J. Jeong and J. Jurng, *Microporous Mesoporous Mater.*, 2012, **163**, 96–101.
- 39 R. Guo, Q. Wang, W. Pan, W. Zhen, Q. Chen, H. Ding, N. Yang and C. Lu, *Appl. Surf. Sci.*, 2014, **317**, 111–116.
- 40 S. S. R. Putluru, L. Schill, A. D. Jensen, B. Siret, F. Tabaries and R. Fehrmann, *Appl. Catal., B*, 2015, **165**, 628–635.
- 41 W. Li, R. Guo, S. Wang, W. Pan, Q. Chen, M. Li, P. Sun and S. Liu, *Fuel Process. Technol.*, 2016, **154**, 235–242.
- 42 B. Thirupathi and P. G. Smirniotis, *J. Catal.*, 2012, **288**, 74–83.
- 43 S. M. Lee, K. H. Park, S. S. Kim, D. W. Kwon and S. C. Hong, *J. Air Waste Manage. Assoc.*, 2012, **62**, 1085–1092.
- 44 J. Luo, Q. Zhang, J. Garcia-Martinez and S. L. Suib, *J. Am. Chem. Soc.*, 2008, **130**, 3198–3207.
- 45 T. Seiyama, *Catal. Rev.*, 1992, **34**, 281–300.
- 46 M. Dhakad, S. S. Rayalu, R. Kumar, P. Doggali, S. Bakardjieva, J. Subrt, T. Mitsunashi, H. Haneda and N. Labhsetwar, *Catal. Lett.*, 2008, **121**, 137–143.
- 47 S. Cimino, L. Lisi and M. Tortorelli, *Chem. Eng. J.*, 2016, **283**, 223–230.
- 48 Z. Wu, R. Jin, H. Wang and Y. Liu, *Catal. Commun.*, 2009, **10**, 935–939.
- 49 P. Sun, R. Guo, S. Liu, S. Wang, W. Pan and M. Li, *Appl. Catal., A*, 2017, **531**, 129–138.
- 50 H. Hu, K. Zha, H. Li, L. Shi and D. Zhang, *Appl. Surf. Sci.*, 2016, **387**, 921–928.
- 51 B. Jiang, Z. Li and S. Lee, *Chem. Eng. J.*, 2013, **225**, 52–58.
- 52 S. Wang, R. Guo, W. Pan, Q. Chen, P. Sun, M. Li and S. Liu, *Catal. Commun.*, 2017, **89**, 143–147.
- 53 L. Ma, Y. Cheng, G. Cavataio, R. W. McCabe, L. Fu and J. Li, *Appl. Catal., B*, 2014, **156–157**, 428–437.
- 54 Z. Wu, B. Jiang, Y. Liu, H. Wang and R. Jin, *Environ. Sci. Technol.*, 2007, **41**, 5812–5817.
- 55 L. Wei, S. Cui, H. Guo and L. Zhang, *Comput. Mater. Sci.*, 2018, **144**, 216–222.
- 56 M. Devadas, O. Kröcher, M. Elsener, A. Wokaun, G. Mitrikas, N. Söger, M. Pfeifer, Y. Demel and L. Mussmann, *Catal. Today*, 2007, **119**, 137–144.
- 57 F. Liu and H. He, *J. Phys. Chem. C*, 2010, **114**, 16929–16936.
- 58 L. Wei, S. Cui, H. Guo, X. Ma and L. Zhang, *J. Mol. Catal. A: Chem.*, 2016, **421**, 102–108.
- 59 E. Tronconi, I. Nova, C. Ciardelli, D. Chatterjee and M. Weibel, *J. Catal.*, 2007, **245**, 1–10.
- 60 H. Hu, S. Cai, H. Li, L. Huang, L. Shi and D. Zhang, *ACS Catal.*, 2015, **5**, 6069–6077.
- 61 H. I. Konstantin, *Catal. Rev.*, 2000, **42**, 71–144.

